



# The two redox states of the human NEET proteins' [2Fe–2S] clusters

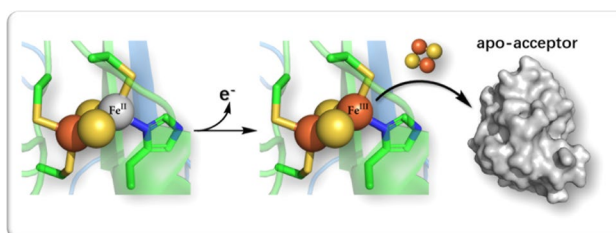
Ke Zuo<sup>1,2</sup> · Henri-Baptiste Marjault<sup>1,2</sup> · Kara L. Bren<sup>3</sup> · Giulia Rossetti<sup>4,5,6</sup> · Rachel Nechushtai<sup>1</sup> · Paolo Carloni<sup>2,4,7</sup>

Received: 14 June 2021 / Accepted: 26 July 2021 / Published online: 28 August 2021  
© The Author(s) 2021

## Abstract

The NEET proteins constitute a unique class of [2Fe–2S] proteins. The metal ions bind to three cysteines and one histidine. The proteins' clusters exist in two redox states; the oxidized protein (containing two Fe<sup>III</sup> ions) can transfer the cluster to apo-acceptor protein(s), while the reduced form (containing one ferrous ion) remains bound to the protein frame. Here, we perform *in silico* and *in vitro* studies on human NEET proteins in both reduced and oxidized forms. Quantum chemical calculations on all available human NEET proteins structures suggest that reducing the cluster weakens the Fe–N<sup>His</sup> and Fe–S<sup>Cys</sup> bonds, similar to what is seen in other Fe–S proteins (e.g., ferredoxin and Rieske protein). We further show that the extra electron in the [2Fe–2S]<sup>+</sup> clusters of one of the NEET proteins (mNT) is localized on the His-bound iron ion, consistently with our previous spectroscopic studies. Kinetic measurements demonstrate that the mNT [2Fe–2S]<sup>+</sup> is released only by an increase in temperature. Thus, the reduced state of human NEET proteins [2Fe–2S] cluster is kinetically inert. This previously unrecognized kinetic inertness of the reduced state, along with the reactivity of the oxidized state, is unique across all [2Fe–2S] proteins. Finally, using a coevolutionary analysis, along with molecular dynamics simulations, we provide insight on the observed allostery between the loop L2 and the cluster region. Specifically, we show that W75, R76, K78, K79, F82 and G85 in the latter region share similar allosteric characteristics in both redox states.

## Graphic abstract



**Keywords** Iron–sulfur cluster lability · Ab initio calculations · Kinetic measurements · Human NEET proteins · Evolutionary analysis

## Introduction

Two iron–two sulfur [2Fe–2S] proteins perform electron transfer, serve as oxygen/iron sensors and transcription factors, and perform enzymatic reactions and many other functions across the three kingdoms of life [1, 2]. They contain a ferrous and ferric or two ferric ions in their reduced and oxidized forms, respectively [3]. The metal ions bind usually to four Cys residues. Yet, in few cases, Asp, Arg and/or His residues [4] replace one or two cysteines (Chart 1). Among these are the

Ke Zuo and Henri-Baptiste Marjault contributed equally.

✉ Rachel Nechushtai  
rachel@mail.huji.ac.il

✉ Paolo Carloni  
p.carloni@fz-juelich.de

Extended author information available on the last page of the article

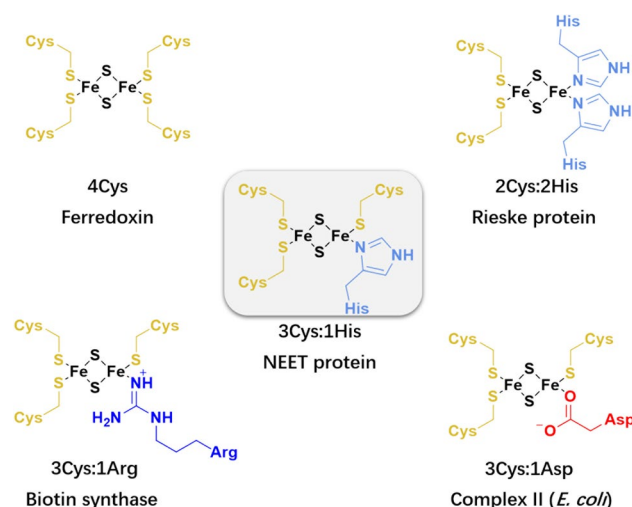


**Chart 1** Metals' coordination in [2Fe–2S] proteins

NEET proteins, featuring two clusters with 3Cys:1His coordination (Chart 1) [5].

Three human NEET proteins have been identified. One (MiNT) is located only inside the mitochondria [6]. The other two, mNT and NAF-1 are anchored to the outer mitochondrial membrane with NAF-1 also present on the surface of the endoplasmic reticulum and its mitochondrial associated membrane [6]. Under healthy conditions [7], they are usually in their reduced, dormant state [8, 9], because of their reducing environment. In the oxidized state, often triggered by oxidative stress [6], the human NEET proteins are able to transfer their [2Fe–2S] clusters to apo-acceptor proteins without the aid of specific chaperons [10] such as the mitochondrial human GLRX5 [11, 12] and the cytosolic human GLRX3 [13] [2Fe–2S] proteins. Unfortunately, aberrant cluster transfer upon oxidative conditions can occur during pathological conditions as in cancer, metabolic and neurodegenerative diseases [6]. Hence, human NEET proteins are promising targets for treating a variety of diseases, from cancer to neurodegenerative diseases [6].

The electronic and structural properties of human oxidized NEET proteins [14, 15], along with their kinetic properties [10, 16], have been characterized. Here, by performing density functional theory (DFT) calculations, molecular dynamics (MD) simulations and in vitro experiments on the reduced and oxidized forms, along with a coevolutionary analysis of these proteins, we provide insight on the reduced state and offer a detailed comparison between the two redox states of the human NEET proteins.

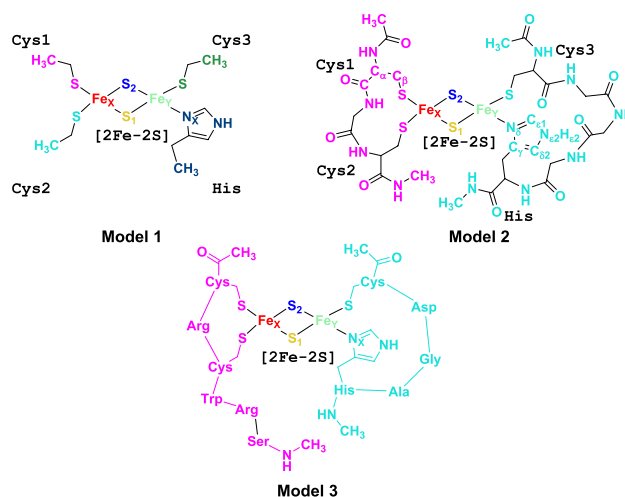


**Fig. 1** Schematic of models 1, 2 and 3 used for the QM calculations presented in this work. In 1, 2 and 3, the [2Fe–2S] clusters are separated into four independent fragments as in Ref. [17] ( $\text{Fe}_X$ ,  $\text{Fe}_Y$ ,  $\text{S}_1$  and  $\text{S}_2$  in the figure). The ligation residues are treated as separate four, two and two fragments in 1, 2 and 3, respectively [17]. The fragments are colored differently

## Results and discussion

Our investigation is carried out in three steps. First, we perform DFT calculations on three models of the reduced metal sites (Fig. 1) to investigate their electronic properties. This work builds on our previous DFT investigations of the oxidized state [17] and it presents also new results for the latter. Next, we perform kinetic measurements to investigate the lability of the reduced cluster at different temperatures. Finally, we carry out a coevolutionary analysis, based on molecular dynamics (MD) simulations on the oxidized and reduced forms performed in this work, to provide insight on the identified allostery between a loop opposed to the cluster (L2 in Fig. 5C) and the cluster binding region [18].

## Quantum chemistry

Calculations at the B3LYP/6–311++G(2d,2p) [19, 20] level of theory (already used for Fe–S proteins [21], including oxidized human NEET proteins [17]) are carried out on all of the 12 human NEET PDB structures (Table S1 and Fig. 1), in both the reduced and oxidized states. These are ten mNT and two NAF-1 proteins. Some of results for the oxidized state have been already reported in Ref. [17].

**Table 1** Average bond lengths ( $R_{\min}$ , in nm) and bond force constants ( $K_r$ , in kJ/mol nm<sup>2</sup>) of [2Fe–2S] clusters as obtained by geometry optimizations of model **1**, based on the human mNT structure (PDB ID: 2QH7<sup>22</sup>)

| Bond   | $R_{\min}$   | $K_r$           | Bond                               | $R_{\min}$   | $K_r$           |
|--|--------------|-----------------|------------------------------------|--------------|-----------------|
| B3LYP, with protonated Fe-bound His (RMSD=0.004/0.014 nm)        |              |                 |                                    |              |                 |
| Fe <sub>X</sub> –S <sub>1</sub>                                  | <b>0.228</b> | <b>31,254.5</b> | Fe <sub>X</sub> –S <sup>Cys1</sup> | <b>0.232</b> | <b>33,555.7</b> |
| Fe <sub>X</sub> –S <sub>2</sub>                                  | <b>0.229</b> | <b>29,497.2</b> | Fe <sub>X</sub> –S <sup>Cys2</sup> | <b>0.232</b> | <b>33,095.4</b> |
| Fe <sub>Y</sub> –S <sub>1</sub>                                  | <b>0.221</b> | <b>46,358.7</b> | Fe <sub>Y</sub> –S <sup>Cys3</sup> | <b>0.233</b> | <b>31,882.1</b> |
| Fe <sub>Y</sub> –S <sub>2</sub>                                  | <b>0.221</b> | <b>45,145.4</b> | Fe <sub>Y</sub> –N <sup>His</sup>  | <b>0.218</b> | <b>16,359.4</b> |
| Fe <sub>X</sub> –S <sub>1</sub>                                  | <i>0.226</i> | <i>36,024.2</i> | Fe <sub>X</sub> –S <sup>Cys1</sup> | <i>0.240</i> | <i>23,472.2</i> |
| Fe <sub>X</sub> –S <sub>2</sub>                                  | <i>0.227</i> | <i>35,187.4</i> | Fe <sub>X</sub> –S <sup>Cys2</sup> | <i>0.240</i> | <i>23,263.0</i> |
| Fe <sub>Y</sub> –S <sub>1</sub>                                  | <i>0.230</i> | <i>30,585.0</i> | Fe <sub>Y</sub> –S <sup>Cys3</sup> | <i>0.242</i> | <i>17,572.8</i> |
| Fe <sub>Y</sub> –S <sub>2</sub>                                  | <i>0.231</i> | <i>29,078.8</i> | Fe <sub>Y</sub> –N <sup>His</sup>  | <i>0.230</i> | <i>7740.4</i>   |
| B3LYP, with unprotonated Fe-bound His (RMSD=0.007/0.006 nm)      |              |                 |                                    |              |                 |
| Fe <sub>X</sub> –S <sub>1</sub>                                  | <b>0.227</b> | <b>34,267.0</b> | Fe <sub>X</sub> –S <sup>Cys1</sup> | <b>0.236</b> | <b>27,154.2</b> |
| Fe <sub>X</sub> –S <sub>2</sub>                                  | <b>0.226</b> | <b>34,225.1</b> | Fe <sub>X</sub> –S <sup>Cys2</sup> | <b>0.234</b> | <b>29,999.3</b> |
| Fe <sub>Y</sub> –S <sub>1</sub>                                  | <b>0.225</b> | <b>35,982.4</b> | Fe <sub>Y</sub> –S <sup>Cys3</sup> | <b>0.236</b> | <b>27,196.0</b> |
| Fe <sub>Y</sub> –S <sub>2</sub>                                  | <b>0.226</b> | <b>35,522.2</b> | Fe <sub>Y</sub> –N <sup>His</sup>  | <b>0.205</b> | <b>32,300.5</b> |
| Fe <sub>X</sub> –S <sub>1</sub>                                  | <i>0.225</i> | <i>39,413.3</i> | Fe <sub>X</sub> –S <sup>Cys1</sup> | <i>0.246</i> | <i>17,028.9</i> |
| Fe <sub>X</sub> –S <sub>2</sub>                                  | <i>0.225</i> | <i>38,534.6</i> | Fe <sub>X</sub> –S <sup>Cys2</sup> | <i>0.243</i> | <i>19,706.6</i> |
| Fe <sub>Y</sub> –S <sub>1</sub>                                  | <i>0.237</i> | <i>21,212.9</i> | Fe <sub>Y</sub> –S <sup>Cys3</sup> | <i>0.246</i> | <i>13,012.2</i> |
| Fe <sub>Y</sub> –S <sub>2</sub>                                  | <i>0.237</i> | <i>20,878.2</i> | Fe <sub>Y</sub> –N <sup>His</sup>  | <i>0.217</i> | <i>14,644.0</i> |
| B(5%HF)P86, with protonated Fe-bound His (RMSD=0.005/0.017 nm)   |              |                 |                                    |              |                 |
| Fe <sub>X</sub> –S <sub>1</sub>                                  | <b>0.224</b> | <b>32,384.2</b> | Fe <sub>X</sub> –S <sup>Cys1</sup> | <b>0.230</b> | <b>31,923.9</b> |
| Fe <sub>X</sub> –S <sub>2</sub>                                  | <b>0.225</b> | <b>30,961.6</b> | Fe <sub>X</sub> –S <sup>Cys2</sup> | <b>0.231</b> | <b>31,338.2</b> |
| Fe <sub>Y</sub> –S <sub>1</sub>                                  | <b>0.219</b> | <b>45,563.8</b> | Fe <sub>Y</sub> –S <sup>Cys3</sup> | <b>0.231</b> | <b>31,589.2</b> |
| Fe <sub>Y</sub> –S <sub>2</sub>                                  | <b>0.219</b> | <b>43,890.2</b> | Fe <sub>Y</sub> –N <sup>His</sup>  | <b>0.216</b> | <b>15,020.6</b> |
| Fe <sub>X</sub> –S <sub>1</sub>                                  | <i>0.225</i> | <i>36,191.6</i> | Fe <sub>X</sub> –S <sup>Cys1</sup> | <i>0.238</i> | <i>24,016.2</i> |
| Fe <sub>X</sub> –S <sub>2</sub>                                  | <i>0.225</i> | <i>35,689.5</i> | Fe <sub>X</sub> –S <sup>Cys2</sup> | <i>0.237</i> | <i>23,848.8</i> |
| Fe <sub>Y</sub> –S <sub>1</sub>                                  | <i>0.224</i> | <i>35,438.5</i> | Fe <sub>Y</sub> –S <sup>Cys3</sup> | <i>0.236</i> | <i>20,836.3</i> |
| Fe <sub>Y</sub> –S <sub>2</sub>                                  | <i>0.225</i> | <i>32,969.9</i> | Fe <sub>Y</sub> –N <sup>His</sup>  | <i>0.223</i> | <i>5230.0</i>   |
| B(5%HF)P86, with unprotonated Fe-bound His (RMSD=0.008/0.007 nm) |              |                 |                                    |              |                 |
| Fe <sub>X</sub> –S <sub>1</sub>                                  | <b>0.223</b> | <b>36,442.6</b> | Fe <sub>X</sub> –S <sup>Cys1</sup> | <b>0.235</b> | <b>27,279.7</b> |
| Fe <sub>X</sub> –S <sub>2</sub>                                  | <b>0.223</b> | <b>36,861.0</b> | Fe <sub>X</sub> –S <sup>Cys2</sup> | <b>0.232</b> | <b>30,375.8</b> |
| Fe <sub>Y</sub> –S <sub>1</sub>                                  | <b>0.223</b> | <b>37,363.1</b> | Fe <sub>Y</sub> –S <sup>Cys3</sup> | <b>0.235</b> | <b>26,986.8</b> |
| Fe <sub>Y</sub> –S <sub>2</sub>                                  | <b>0.224</b> | <b>36,484.5</b> | Fe <sub>Y</sub> –N <sup>His</sup>  | <b>0.204</b> | <b>31,212.6</b> |
| Fe <sub>X</sub> –S <sub>1</sub>                                  | <i>0.224</i> | <i>38,785.7</i> | Fe <sub>X</sub> –S <sup>Cys1</sup> | <i>0.245</i> | <i>17,321.8</i> |
| Fe <sub>X</sub> –S <sub>2</sub>                                  | <i>0.224</i> | <i>38,409.1</i> | Fe <sub>X</sub> –S <sup>Cys2</sup> | <i>0.240</i> | <i>20,459.8</i> |
| Fe <sub>Y</sub> –S <sub>1</sub>                                  | <i>0.230</i> | <i>25,355.0</i> | Fe <sub>Y</sub> –S <sup>Cys3</sup> | <i>0.240</i> | <i>15,522.6</i> |
| Fe <sub>Y</sub> –S <sub>2</sub>                                  | <i>0.231</i> | <i>24,685.6</i> | Fe <sub>Y</sub> –N <sup>His</sup>  | <i>0.215</i> | <i>14,309.3</i> |

As mentioned above, the geometry optimizations of the 12 X-ray structures lead to very similar structural determinants. Thus, only the results for one of them (PDB ID: 2QH7 [22]) are reported here. The calculations are carried out at the B3LYP/6-311++G(2d,2p) [19, 20] (top) and B(5%HF)P86/def-TZVP [23, 24] (bottom) levels. Both the oxidized (in bold face) and reduced (in italics) states are considered. The protonation state of the iron-bound histidine is specified in the table. The overall RMSD relative to the initial structures are reported in parentheses

The calculations shed light on the strength of the Fe–N<sup>His</sup> and Fe–S<sup>Cys</sup> bonds upon reduction: the force constants and delocalization indexes, which correlate with bond strengths and bond orders [25], respectively, decrease (Tables 1, 2, and S3). The Fe-bound His is considered here to be protonated (Fig. 2A). Similar conclusions are drawn: (i) when considering the His to be deprotonated (Table 2); (ii) when including the protein frame's electric field and thermal fluctuations of the protein using results from MD simulations performed in this work (see “Methods”); (iii) when employing another functional used for Fe–S proteins [B(5%HF)P86/def-TZVP] [23, 24, 26]; (iv) when including dispersion contributions, which can be significant in DFT calculations on proteins [27]. Thus, these results appear to be quite robust. They are fully consistent with previous studies which point to a decrease of iron-donor atom bond strength upon the reduction of 4Cys-coordinated [28] and 2Cys:2His [2Fe–2S] proteins [29].

Our QM calculations provide information also into the change in charge distribution in the cluster. The extra charge density turns out to involve the His-bound iron ion, close to the protein surface, and its ligands (Fig. 2A). Indeed, the largest increase in electronic charge is mainly localized on that iron ion, on the two inorganic sulfurs and the histidine. Interestingly, however, the nitrogen donor atom decreases its charge. This is likely to be caused by a competition between the Fe–N<sup>His</sup>  $\sigma$  bond, which may be stronger in the oxidized state [33], and the  $\pi$  bond involving the aromatic ring and the metal ion. An analysis of the localized orbital locator (LOL) values on the critical points, which correlate with bond strength [30], suggests that this is the case. Indeed, on passing from the oxidized to the reduced forms, the LOL  $\sigma$  values decrease from 0.21 to 0.19, while the LOL  $\pi$  values increase from 0.15 to 0.24, overcoming the contribution of the  $\sigma$  donation (Figs. 2B and S1). The reduction process is carried by the lowest unoccupied molecular orbital (LUMO) of the oxidized form, ready to accept the electron upon reduction, and the highest occupied MO (HOMO) of the reduced form; both are mainly localized on the His-bound iron ion, close to the protein surface, but not the other iron ion (Figs. 2C and S2–S6). We conclude that the His-bound iron, located at the surface of the protein, is the one that gets reduced. This is fully consistent with spectroscopic studies, which show that the reduced form features a ferrous iron bound to His87 [14]. We close this section by pointing out that one of the three human NEET proteins, mNT, exhibits highly complex proton coupled electron transfer processes during reduction [16], although a clear link between these processes and cluster release has not emerged yet. This process is not investigated here: we rather focus on the

**Table 2** Delocalization indexes of the Fe–N<sup>His</sup> and Fe–S bond in oxidized (top line, bold face) and reduced (bottom line, italics) states, respectively

|                     | Fe <sub>X</sub> –S <sup>Cys1</sup> | Fe <sub>X</sub> –S <sup>Cys2</sup> | Fe <sub>X</sub> –S <sub>1</sub> | Fe <sub>X</sub> –S <sub>2</sub> | Fe <sub>Y</sub> –S <sup>Cys3</sup> | Fe <sub>Y</sub> –N <sup>His</sup> | Fe <sub>Y</sub> –S <sub>1</sub> | Fe <sub>Y</sub> –S <sub>2</sub> |
|---------------------|------------------------------------|------------------------------------|---------------------------------|---------------------------------|------------------------------------|-----------------------------------|---------------------------------|---------------------------------|
| B3LYP geometry      | Protonated His                     |                                    |                                 |                                 |                                    |                                   |                                 |                                 |
|                     | <b>0.567</b>                       | <b>0.553</b>                       | <b>0.610</b>                    | <b>0.590</b>                    | <b>0.544</b>                       | <b>0.281</b>                      | <b>0.755</b>                    | <b>0.736</b>                    |
|                     | <i>0.476</i>                       | <i>0.471</i>                       | <i>0.685</i>                    | <i>0.677</i>                    | <i>0.457</i>                       | <i>0.234</i>                      | <i>0.579</i>                    | <i>0.557</i>                    |
|                     | <b>0.583<sup>†</sup></b>           | <b>0.564<sup>†</sup></b>           | <b>0.603<sup>†</sup></b>        | <b>0.602<sup>†</sup></b>        | <b>0.557<sup>†</sup></b>           | <b>0.306<sup>†</sup></b>          | <b>0.742<sup>†</sup></b>        | <b>0.745<sup>†</sup></b>        |
|                     | <i>0.491<sup>†</sup></i>           | <i>0.486<sup>†</sup></i>           | <i>0.686<sup>†</sup></i>        | <i>0.672<sup>†</sup></i>        | <i>0.466<sup>†</sup></i>           | <i>0.269<sup>†</sup></i>          | <i>0.575<sup>†</sup></i>        | <i>0.560<sup>†</sup></i>        |
|                     | Deprotonated His                   |                                    |                                 |                                 |                                    |                                   |                                 |                                 |
|                     | <b>0.524<sup>†</sup></b>           | <b>0.533<sup>†</sup></b>           | <b>0.651<sup>†</sup></b>        | <b>0.647<sup>†</sup></b>        | <b>0.522<sup>†</sup></b>           | <b>0.410<sup>†</sup></b>          | <b>0.658<sup>†</sup></b>        | <b>0.648<sup>†</sup></b>        |
|                     | <i>0.442<sup>†</sup></i>           | <i>0.459<sup>†</sup></i>           | <i>0.721<sup>†</sup></i>        | <i>0.709<sup>†</sup></i>        | <i>0.440<sup>†</sup></i>           | <i>0.353<sup>†</sup></i>          | <i>0.506<sup>†</sup></i>        | <i>0.497<sup>†</sup></i>        |
| B(5%HF)P86 geometry | Protonated His                     |                                    |                                 |                                 |                                    |                                   |                                 |                                 |
|                     | <b>0.633</b>                       | <b>0.579</b>                       | <b>0.730</b>                    | <b>0.734</b>                    | <b>0.570</b>                       | <b>0.426</b>                      | <b>0.740</b>                    | <b>0.723</b>                    |
|                     | <i>0.482</i>                       | <i>0.483</i>                       | <i>0.694</i>                    | <i>0.687</i>                    | <i>0.484</i>                       | <i>0.257</i>                      | <i>0.619</i>                    | <i>0.590</i>                    |
|                     | <b>0.562</b>                       | <b>0.563</b>                       | <b>0.648</b>                    | <b>0.625</b>                    | <b>0.542</b>                       | <b>0.296</b>                      | <b>0.754</b>                    | <b>0.745</b>                    |
|                     | <i>0.475</i>                       | <i>0.491</i>                       | <i>0.704</i>                    | <i>0.668</i>                    | <i>0.473</i>                       | <i>0.275</i>                      | <i>0.599</i>                    | <i>0.612</i>                    |
|                     | Deprotonated His                   |                                    |                                 |                                 |                                    |                                   |                                 |                                 |
|                     | <b>0.516</b>                       | <b>0.537</b>                       | <b>0.659</b>                    | <b>0.665</b>                    | <b>0.515</b>                       | <b>0.403</b>                      | <b>0.682</b>                    | <b>0.668</b>                    |
|                     | <i>0.425</i>                       | <i>0.454</i>                       | <i>0.729</i>                    | <i>0.720</i>                    | <i>0.451</i>                       | <i>0.335</i>                      | <i>0.542</i>                    | <i>0.528</i>                    |
|                     | <b>0.515</b>                       | <b>0.531</b>                       | <b>0.680</b>                    | <b>0.658</b>                    | <b>0.514</b>                       | <b>0.398</b>                      | <b>0.675</b>                    | <b>0.664</b>                    |
|                     | <i>0.429</i>                       | <i>0.458</i>                       | <i>0.737</i>                    | <i>0.705</i>                    | <i>0.448</i>                       | <i>0.327</i>                      | <i>0.544</i>                    | <i>0.535</i>                    |

These have been obtained by unrestricted HF/6-311++G(2d,2p) calculations on model **1** as in Ref. [25], based on the B3LYP/6-311++G(2d,2p) [19, 20] and B(5%HF)P86/def-TZVP [23, 24] optimized structures. The geometry optimizations are carried out either without constraints or with constraints on the C<sub>α</sub> atoms (underscored number). Numbers with a dagger symbol were obtained by adding DFT-D3(BJ) corrections [27, 31, 32] in geometry optimizations (see “Methods”). Because the latter are almost identical across the structures investigated here, the results of only one of them (Human mNT, PDB ID: 2QH7 [22]) are reported

initial and final states of the process (i.e., four possible oxidized/reduced [2Fe–2S] with protonated/deprotonated His ligand states, see Fig. 2A).

### Kinetic measurements

The reduced state is inert at room temperature [16]. So, we expect that the free energy barrier of cluster transfer is higher at the transition state in the reduced form ( $\Delta G_{\text{red}}^{\ddagger} > \Delta G_{\text{ox}}^{\ddagger}$ , see Fig. 3). To test this hypothesis, we measured the in vitro stability of the [2Fe–2S] clusters of the wild type mNT protein as well as H87C variant in the reduced state at different temperatures (Figs. 4 and S7). For a proper comparison with the oxidized state, we perform the measurements for the oxidized state (already reported in Ref. [10]), in exactly the same conditions as those carried out for the reduced form. The oxidized [2Fe–2S] clusters are highly labile at 310 K, as already observed [16] ( $\Delta G_{\text{ox}}^{\ddagger} \approx k_B T$ ) while the reduced ones remain stable over a long time in the same conditions (Fig. 4A). Thus, here  $\Delta G_{\text{red}}^{\ddagger} > k_B T$ . However, the lability of the reduced correlates with the rise of temperature to 313, 315 and 318 K (Fig. 4B). Taking these results together with those of the previous section, we suggest that reduction weakens the coordination bonds but the cluster stays bound to the protein at physiological temperature because of

a relatively high free energy barrier that hampers its release (Fig. 4); i.e., the reaction is kinetically controlled. On the other hand, the oxidized state, albeit more thermodynamically stable, is labile at room temperature because of the small barrier to release (Fig. 4). Interestingly, increasing the temperature turns out not affect the cluster lability of the H87C mutant, in which the Fe-bound histidine is replaced by a cysteine (Fig. S7). Thus, the His-Fe bound is a key determinant for the observed reactivity of the cluster at higher temperature.

### Coevolutionary analysis and molecular dynamics simulations

So far, our attention has focused on specific properties of the cluster, from the electronic structure to kinetics. We close this section by investigating an important property involving the *entire* protein, in both the reduced and oxidized states. This is the allostery between L2 present in mNT’s β-cap domain and the cluster binding region, which was observed by one of us many years ago [35]. This allostery plays an essential role in the cluster release/transfer to apo-acceptor proteins [8, 35]. Here, we identify the specific residues involved in the allostery as well as the dependence of the

latter on the redox state of the protein. Both features are currently not known.

Here, we exploit the fact that allosteric communication between different protein regions can be mirrored by pairs of coevolved residues [18]. These residues exhibit concordant patterns of evolution: they jointly mutated with a frequency higher than the average [36]. A pair of residues is considered to be strongly coevolving if the residues are not in close proximity of each other and if their coevolution score (here calculated with the CoeViz web server (<http://polyview.cchmc.org/>) [18] is greater than 0.7. The calculation of the co-evolution score is based on proteins' sequences [18]. To determine the contiguity between the residue pairs, we need structural information on the reduced and oxidized mNT. Because the experimental structure of the reduced form is not available [37], here we use representative structures from 1  $\mu$ s long, AMBER-based MD simulations of the oxidized and reduced mNT in solution (see SI, Section III). The simulations are based on the X-ray structure of mNT (PDB ID: 2QH7 [22]). They use an AMBER-compatible force fields developed here and in Ref. [17] for the reduced and oxidized metal clusters, respectively.

The identified strong coevolving pairs are the same for both redox states (Fig. S12), consistent with the high similarity between reduced and oxidized mNT representative MD structures: the RMSD on the  $C_\alpha$  atoms is as low as 0.5 Å (see Fig. S10). In particular, Trp75, Arg76, Lys78 and Lys79 adjacent to cluster binding area, along with Phe82 and Gly85 located beside ligand Cys83 and His87, turn out to strongly co-evolve with Met62–Lys68 in L2 region, and, the latter two, also with Cys83 and His87 (Figs. 5 and S12).<sup>1</sup> Thus, our analysis confirms previous findings [35], and details which residues are involved in the allosteric communication. Our analysis shows that the cross-talk between the  $\beta$ -cap and cluster binding region of human mNT involves the same amino acid residues in oxidized and in the reduced form. However, the allosteric effect on these amino acids can differ significantly on passing from one oxidation state to the other. These findings do not provide insights into the role that allostery plays in the cluster release/transfer to apo-acceptor proteins or into the redox dependence of cluster release/transfer.

## Conclusions

We have provided here a detailed picture of the reduced form of human NEET proteins and compared it with that of the oxidized state. Our quantum chemical studies, performed across all structures available in the PDB, suggest

that reduction of the oxidized cluster involves the iron bound to the histidine, consistent with experiment [14] and it weakens the coordination bonds of the metal ions, as seen for other iron–sulfur clusters. Nevertheless, the cluster remains bound in the reduced state because it is kinetically inert, as shown here by in vitro measurements on the mNT protein's cluster stability. Finally, our in silico analysis across all human NEET proteins provide insight on the observed allostery cross-talk between the L2 of the  $\beta$ -cap domain and the cluster region [35]. The residues involved in it turn out to be Met62–Lys68, from the L2 loop and Trp75, Arg76, Lys78, Lys79, Phe82 and Gly85 from the cluster region for mNT in both redox states (Figs. 5 and S12).

## Methods

### QM calculations

The MCPB.py script [38] in the AMBER16 package [39] was employed to construct the QM truncated models **1**, **2** and **3** (Fig. 1). These are built from the 12 X-ray structures of human NEET proteins (mNT [22, 35, 40–44] and NAF-1 [45, 46], Table S1). In **1**, the [2Fe–2S] cluster and the side chains of ligated three cysteine residues and one histidine residue were included. All  $C_\beta$ s are saturated with H atoms. In **2**, the whole ligation residues, as mentioned above, and the main chain atoms of the residues connecting those residues in the protein were included. The side chain of connection residues was replaced with H atoms. **3** included the [2Fe–2S] cluster and all residues within 4 Å from the cluster. Models **1** were terminated by methyl groups, those of **2** and **3** with acetyl (ACE) or *N*-methyl (NME) groups. Hydrogen atoms were added assuming standard bond lengths and angles.

The experimental spin state of the NEET proteins was given as an input in the fragment-combination method (Table S2) [47]. This method controls the generation of initial guess for the Hartree–Fock wavefunction from fragment guesses or self-consistent field method solutions, which converged the wavefunction to the desired antiferromagnetic state. It has been used for a variety of other Fe–S proteins [21], including NEET proteins in the oxidized state [17]. Geometry optimization of **1** was carried out with the unrestricted B3LYP/6-311++G(2d,2p) [19, 20] with and without Grimme-type empirical D3(BJ) dispersion corrections [27, 31, 32], and B(5%HF)P86/def-TZVP functionals [23, 24]. Both functionals have been widely used to study [2Fe–2S] and [4Fe–4S] clusters' electronic structure [17, 21, 26].<sup>2</sup> The

<sup>1</sup> The coevolution score of four cluster ligating amino acids with L2 and other regions of the protein is much lower than 0.7.

<sup>2</sup> Several other functionals have been used to investigate Fe–S clusters (for instance PW91 [48] and BP86 [48, 49]).



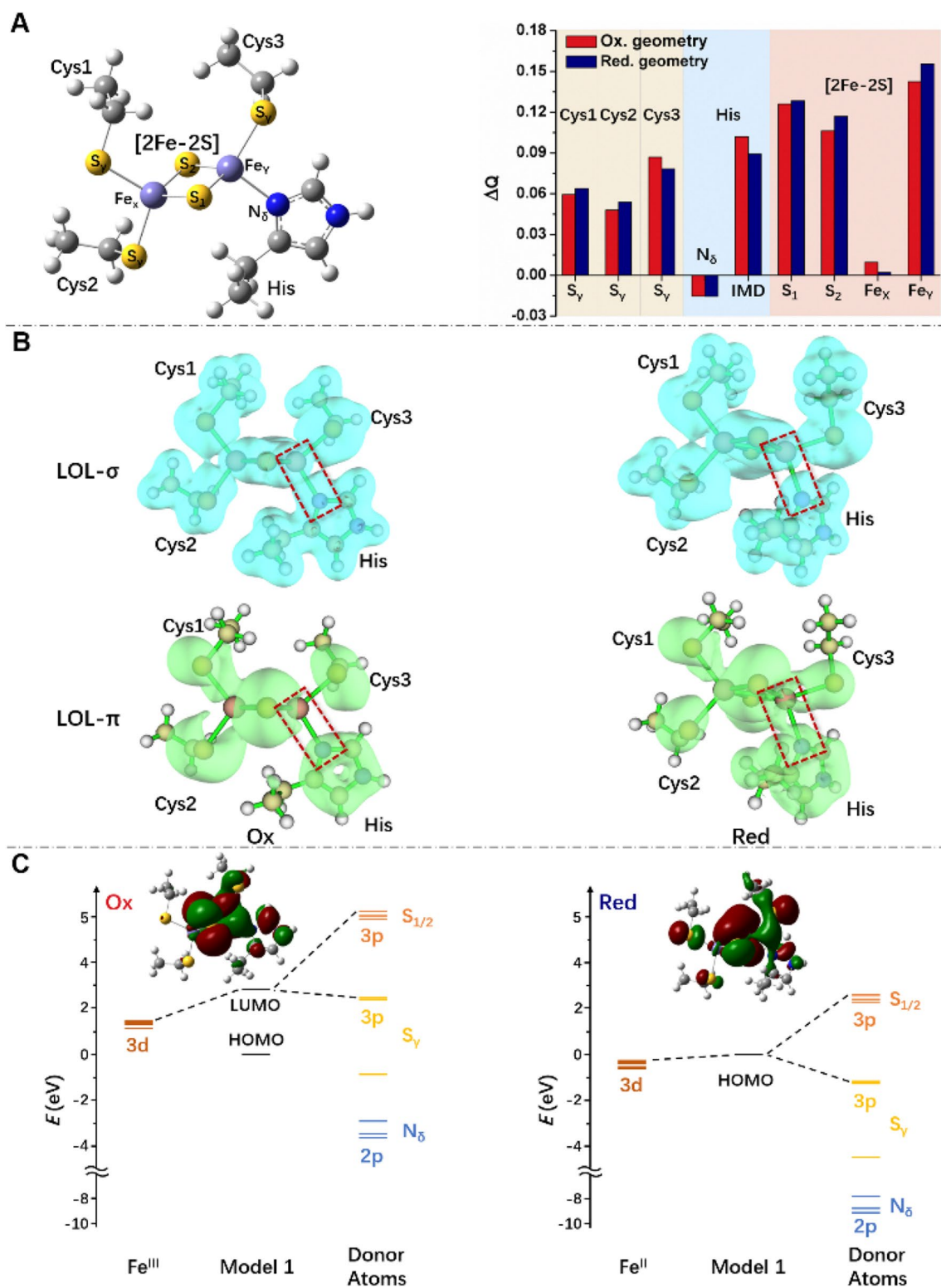


**Fig. 2** The two redox states of the clusters in human NEET proteins. **A** The charge (right) upon reduction of the oxidized state is localized to His-bound iron  $\text{Fe}_\text{V}$ , bridge sulfur  $\text{S}_1$  and  $\text{S}_2$ , and  $\text{S}_\gamma$  of Cys ligands while it decreases on  $\text{N}_8$  of His ligand. **B** Contours ( $0.2 \text{ e}/\text{\AA}^3$ ) of the localized orbital locator (LOL) [30] for the complex and in particular for the histidine-iron  $\sigma$  and  $\pi$  bonds. **C** The molecular orbitals involved in the reduction are the LUMO of the oxidized form and the HOMO of the reduced form, as emerging from an analysis of the Kohn–Sham orbitals. Both involve the surface localized His-bound iron and not the other iron. The HOMO energy is set to zero for each state. Contours shown at  $0.01 \text{ e}/\text{\AA}^3$ . The calculations are carried out at the B3LYP/6-311++G(2d,2p) [19, 20] level of theory for the PDB ID: 2QH7 structure [22]. Very similar results are obtained for all the other 11 structures analyzed here and for calculations at the B(5%HF) P86 [23, 24] level of theory (data not shown)

geometrical optimization was carried out using the following convergence criterion: the maximum and RMS force on the nuclei are less than 0.00045 Hartrees/Bohr and 0.00035 Hartrees/Bohr, respectively, and the maximum and RMS nuclei displacement are less than 0.0018 and 0.0012 Å, respectively. The structural determinants of the optimized structures are basically identical and therefore the results are reported only for the mNT protein (PDB ID: 2QH7 [22]). Single point energy calculations, based on the X-ray structures, were carried out at the unrestricted B3LYP/6-311++G(2d,2p) level [19, 20] on **2** and **3**.

In some calculations, we applied constraints on the  $\text{C}_\alpha$  atoms within geometry optimization to mimic protein environment in model **1**. We finally carried out single point calculations on model **1** with the geometry of cluster representatives of the MD simulations (see section below).

An in-house code (cpmd-cube-tools: <https://pypi.org/project/cpmd-cube-tools/>) [50] was used to calculate the change in electron density ( $\Delta\rho$ ) upon reduction of **1**:

$$\Delta\rho = \rho_{\text{red}} - \rho_{\text{ox}},$$

where  $\rho_{\text{red}}$  and  $\rho_{\text{ox}}$  were the electron densities in the reduced and oxidized states, respectively. The calculations were based on the optimized geometry of the oxidized states. The changes in charge ( $\Delta Q$ ) were calculated as integrals of  $\Delta\rho$  around selected atoms.

## Coevolution analysis

This was performed with the web-based tool CoeViz [18] integrated in the web server POLYVIEW-2D [51]. Weighted Chi-squared metric was used with 20 amino acid alphabets by sequence identity [18, 52]. The cut-off of strong co-evolution was set to 30% top scores based on the statistics of the whole co-evolution scores.

## MD simulations of oxidized and reduced human mNT in water solution

The calculations were based on the X-ray structure with PDB ID: 2QH7 [22]. H atoms were added to the heavy atoms assuming standard bond length and bond angles. The titratable residues were protonated assuming a pH of 6.0—the same as in our experiments below—using the H++ webserver [53]. The proteins were embedded in the center of a dodecahedron box with a distance of 3.0 nm or larger from the protein to the border of the box.  $\text{Na}^+$  and  $\text{Cl}^-$  ions were added to neutralize the systems and mimic our experimental ionic strengths of 100 mM NaCl, (see “Experimental procedure”, Table S5).

The protein, water and counterions were described by the AMBER99SB-ILDN [54, 55], TIP3P [56], and the Åqvist potential [57], respectively. The force field parameters of the clusters were calculated for the reduced state using MCPB.py [38] following Ref. [21] and our previous work [17] (Table 1). In particular, the restrained electrostatic potential (RESP) atomic charges [58] were calculated on **2** using the Merz–Kollman (MK) scheme [59] at the same unrestricted B3LYP/6-311++G(2d,2p) theoretical level [19, 20]. All the parameters are compatible with the AMBER99SB-ILDN force field [54, 55]. For the oxidized state, we used our previous work [17].

Periodic boundary conditions were applied. Particle mesh Ewald (PME) method [60] was used for electrostatic interaction with a cutoff of 1.2 nm. The cutoff used for van der Waals interaction was 1.2 nm. Using the LINCS algorithm [61] to constrain all of the bonds. The Nose–Hoover thermostat [62, 63] and Parrinello–Rahman barostat [64] were used to obtain the constant temperature and pressure conditions, respectively. The integration step of the MD simulation above was set to 2 fs. Each system was energy-minimized by 50,000-step steepest descent and 50,000-step conjugate gradient algorithms, respectively, then heated up to 300 K by 1-ns simulated annealing process. To pre-equilibrate the simulated systems, 50-ns isochoric-isothermal (NVT) and 50-ns isobaric-isothermal (NPT) simulations were employed orderly. Then, 1-μs production trajectories were collected at 310 K and 1 atm for data analyses. Both MD simulations equilibrate after 100 ns (see SI, Fig. S9). We select representative structures from equilibrated trajectories (that is, the last 200 ns) using a cluster analysis (see SI, Section III).

The GROMOS clustering analysis code [65] was employed to identify the representative conformations in the last 200-ns trajectories, with a cutoff of 0.11 nm of backbone. 16 and 8 representatives were obtained for the oxidized and reduced proteins, respectively.

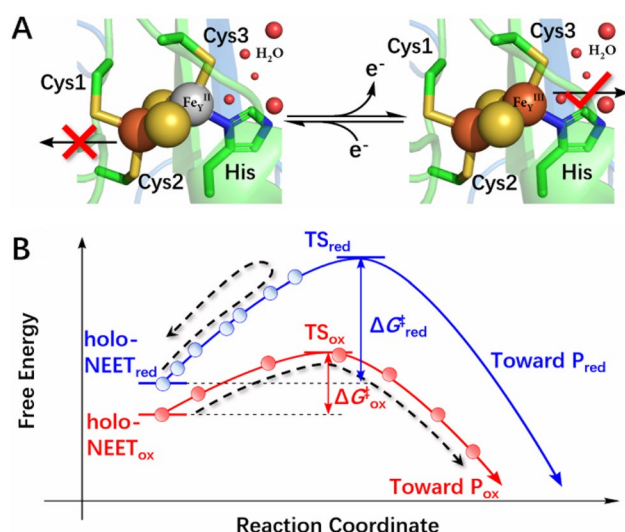


**Fig. 3** Redox-dependent lability of NEET proteins' [2Fe–2S] clusters. **A** The reduced clusters remain stable through a large range of pH [16] (left). Oxidation allows their transfer to an apo-acceptor-protein(s) (right). **B** Proposed free energy landscape associated with the [2Fe–2S] cluster release, described by a generic Reaction Coordinate. Here, the lower free energy of the oxidized state is assumed based on our DFT calculations. TS for transition state, and  $P_{red}$  and  $P_{ox}$  for products [apo-NEET proteins along with the released cluster either to water solution [10] (in vitro) or to their cellular partners [11] (in vivo) in the reduced and oxidized forms, respectively]. The schematic is qualitative

## Codes

QM, molecular orbitals analyses and MD calculations were carried out using in Gaussian09 [47], GaussView5.0 [66], Multiwfn [67], and GROMACS 2019.4 [68, 69] software packages, respectively.

## Experimental procedure

### Proteins expression and purification

mNT protein and its H87C mutant were expressed and purified as described in Refs. [10, 45]. Briefly, the soluble part of mNT protein/H87C (residue 33–108) were inserted into the expression vector pet-28a+ (Novagen). The recombinant human mNT/H87C was expressed in *Escherichia coli* BL21-RIL grown in LB supplemented with 30 µg/mL kanamycin and 34 µg/mL chloramphenicol. At an OD<sub>600</sub> of 0.6, the cells were supplemented with 0.75 mM FeCl<sub>3</sub> and the expression was activated using 0.25 mM of IPTG. Cell growth proceeded for additional 12 h at 310 K. From lysed cells, the mNT

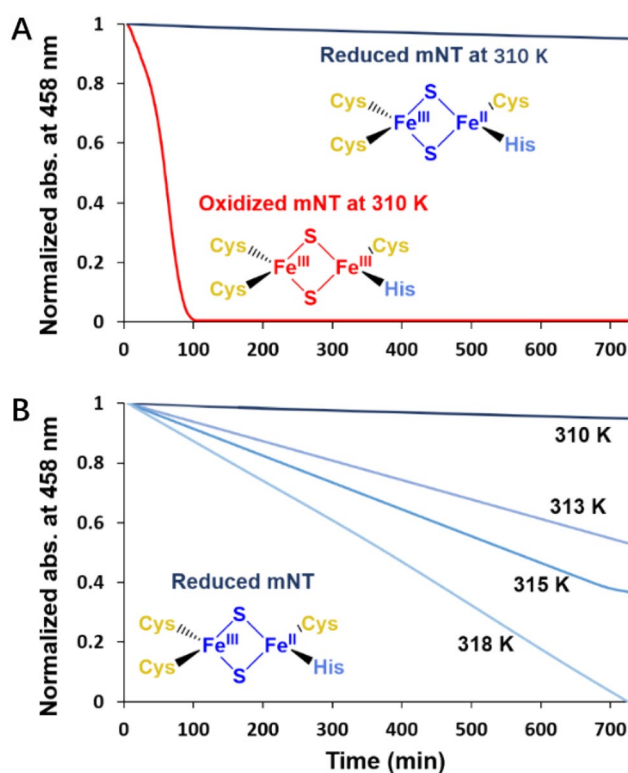


**Fig. 4** Lability of [2Fe–2S] clusters of mNT at different temperatures. The absorbance and stability of the clusters are monitored at their characteristic absorption peak of 458 nm. **A** At 310 K, the oxidized clusters are highly labile and dissociate from the protein (red line), while the reduced clusters are stable (dark blue lines). **B** By increasing the temperature up to 318 K the latter induces a loss of their stability (from dark blue to light blue lines). The measurements have been taken at pH 6.0, which is closer to the physiological pH in pathologies like cancer [34] and renders the reaction in vitro faster than that at pH 8.0

proteins were purified using Ni-agarose and size exclusion chromatography as described in Refs. [10, 22].

### Proteins reduction and in vitro stability kinetics measurement

100 µM mNT protein or H87C mutant were reduced beforehand by degassing the buffer (100 mM Bis-Tris (pH 6.0) and 100 mM NaCl) with nitrogen to remove the O<sub>2</sub> from the solution. mNT/H87C proteins were then reduced using 1 mg of sodium dithionite. Immediately, the proteins (mNT and its mutant) were disposed in a 96-well plate and sealed (to prevent gas exchange). The kinetics of the [2Fe–2S] cluster release of mNT and its mutant, H87C, was monitoring by measuring the specific



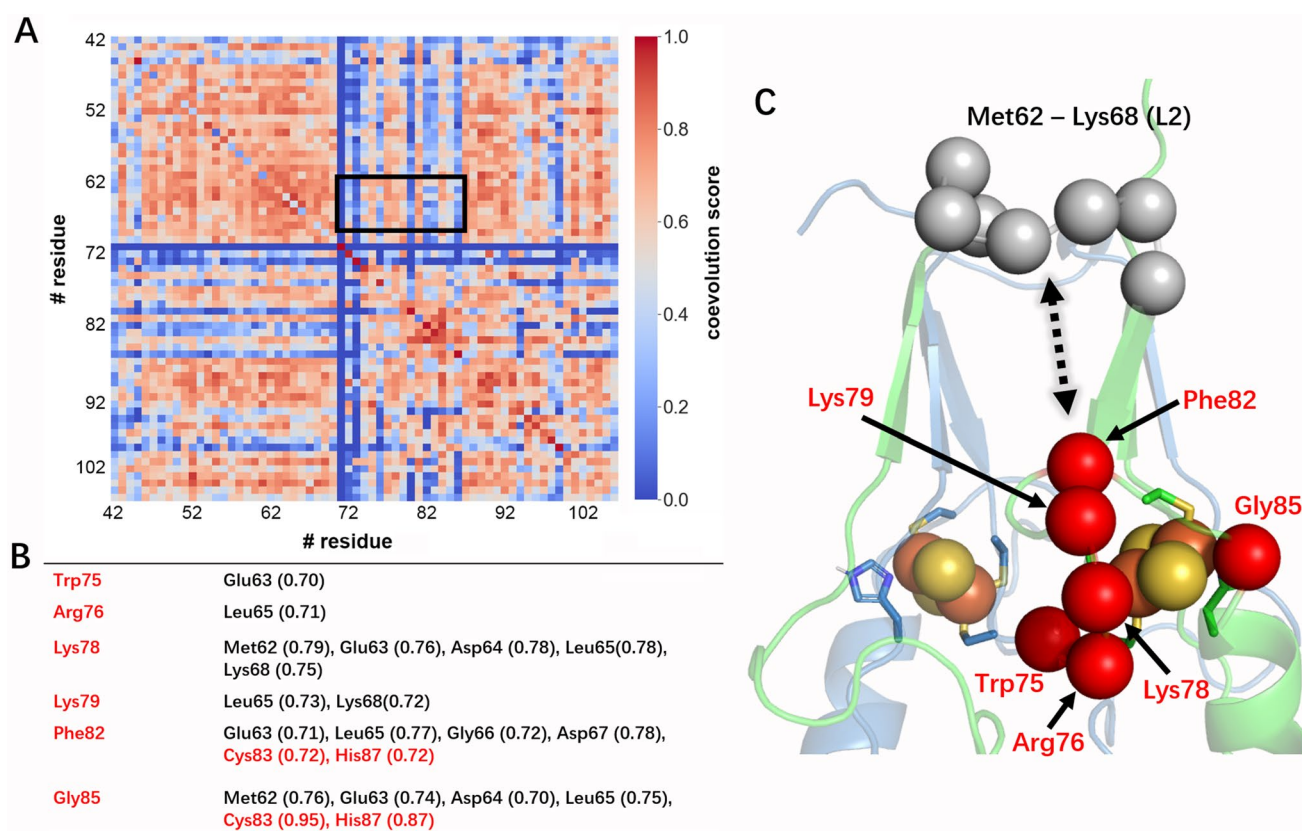


**Fig. 5** Allostery between [2Fe–2S] cluster area and L2 region of the  $\beta$ -cap domain of mNT. **A** The coevolution score heatmap, as obtained by CoeViz [18]. The one in the reduced state is shown in Fig. S12. **B**, **C** Strongly coevolving amino acid pairs from the cluster area and

L2. **B** reports the coevolution scores. **C** shows the location of these residues in oxidized mNT in aqueous solution, as emerging from MD simulation (see SI, Section III). The correspondent structure for the reduced state in solution is shown in Fig. S10

absorption peak of the NEET protein, at 458 nm using Synergy™ H1 plate reader, equipped with a temperature control apparatus set to at 310, 313, 315 and 318 K.

**Supplementary information** The online version contains supplementary material available at <https://doi.org/10.1007/s00775-021-01890-8>.

**Acknowledgements** We thank Maria Ramos for her highly valuable comments. R.N. acknowledge the MINERVA Center for Bio-hybrid Complex Systems. We also acknowledge the computing time granted by RWTH Compute Cluster (no. 3497).

**Author contributions** K.Z. performed the calculations. H.-B.M. performed the in vitro experiment. R.N. and P.C. supervised the project and wrote the paper with input from all authors.

**Funding** Open Access funding enabled and organized by Projekt DEAL. K.Z. and H.-B.M. are supported by the Marie Skłodowska-Curie Grant agreement no. 765048.

## Declarations

**Conflict of interest** The authors declare that they have no conflict of interest.

**Open Access** This article is licensed under a Creative Commons Attribution 4.0 International License, which permits use, sharing, adaptation, distribution and reproduction in any medium or format, as long as you give appropriate credit to the original author(s) and the source, provide a link to the Creative Commons licence, and indicate if changes were made. The images or other third party material in this article are included in the article's Creative Commons licence, unless indicated otherwise in a credit line to the material. If material is not included in the article's Creative Commons licence and your intended use is not permitted by statutory regulation or exceeds the permitted use, you will need to obtain permission directly from the copyright holder. To view a copy of this licence, visit <http://creativecommons.org/licenses/by/4.0/>.

## References

1. Lill R, Freibert SA (2020) Mechanisms of mitochondrial iron–sulfur protein biogenesis. *Annu Rev Biochem* 89:471–499. <https://doi.org/10.1146/annurev-biochem-013118-111540>
2. Dorner K, Vranas M, Schimpf J, Straub IR, Hoer J, Friedrich T (2017) Significance of [2Fe–2S] cluster N1a for electron transfer and assembly of *Escherichia coli* respiratory complex I. *Biochemistry* 56(22):2770–2778. <https://doi.org/10.1021/acs.biochem.6b01058>
3. Anxolabehere-Mallart E, Glaser T, Frank P, Aliverti A, Zanetti G, Hedman B, Hodgson KO, Solomon EI (2001) Sulfur K-edge

- X-ray absorption spectroscopy of 2Fe–2S ferredoxin: covalency of the oxidized and reduced 2Fe forms and comparison to model complexes. *J Am Chem Soc* 123(23):5444–5452. <https://doi.org/10.1021/ja010472t>
4. Ohta S, Ohki Y (2017) Impact of ligands and media on the structure and properties of biological and biomimetic iron–sulfur clusters. *Coord Chem Rev* 338:207–225. <https://doi.org/10.1016/j.ccr.2017.02.018>
  5. Lin JZ, Zhang LM, Lai SM, Ye KQ (2011) Structure and molecular evolution of CDGSH iron–sulfur domains. *PLoS One* 6(9):e24790. <https://doi.org/10.1371/journal.pone.0024790>
  6. Nechushtai R, Karmi O, Zuo K, Marjault HB, Darash-Yahana M, Sohn YS, King SD, Zandalinas SI, Carloni P, Mittler R (2020) The balancing act of NEET proteins: iron, ROS, calcium and metabolism. *Biochim Biophys Acta Mol Cell Res* 1867(11):118805. <https://doi.org/10.1016/j.bbamcr.2020.118805>
  7. Landry AP, Ding HG (2014) Redox control of human mitochondrial outer membrane protein mitoNEET [2Fe–2S] clusters by biological thiols and hydrogen peroxide. *J Biol Chem* 289(7):4307–4315. <https://doi.org/10.1074/jbc.M113.542050>
  8. Camponeschi F, Ciofi-Baffoni S, Banci L (2017) Anamorsin/Ndor1 complex reduces [2Fe–2S]-mitoNEET via a transient protein–protein interaction. *J Am Chem Soc* 139(28):9479–9482. <https://doi.org/10.1021/jacs.7b05003>
  9. Landry AP, Cheng ZS, Ding HG (2015) Reduction of mitochondrial protein mitoNEET [2Fe–2S] clusters by human glutathione reductase. *Free Radic Biol Med* 81:119–127. <https://doi.org/10.1016/j.freeradbiomed.2015.01.017>
  10. Zuris JA, Harir Y, Conlan AR, Shvartsman M, Michaeli D, Tamir S, Paddock ML, Onuchic JN, Mittler R, Cabantchik ZI, Jennings PA, Nechushtai R (2011) Facile transfer of [2Fe–2S] clusters from the diabetes drug target mitoNEET to an apo-acceptor protein. *Proc Natl Acad Sci USA* 108(32):13047–13052. <https://doi.org/10.1073/pnas.1109986108>
  11. Brancaccio D, Gallo A, Piccioli M, Novellino E, Ciofi-Baffoni S, Banci L (2017) [4Fe–4S] Cluster assembly in mitochondria and its impairment by copper. *J Am Chem Soc* 139(2):719–730. <https://doi.org/10.1021/jacs.6b09567>
  12. Brancaccio D, Gallo A, Mikolajczyk M, Zovo K, Palumaa P, Novellino E, Piccioli M, Ciofi-Baffoni S, Banci L (2014) Formation of [4Fe–4S] clusters in the mitochondrial iron–sulfur cluster assembly machinery. *J Am Chem Soc* 136(46):16240–16250. <https://doi.org/10.1021/ja507822j>
  13. Camponeschi F, Prusty NR, Heider SAE, Ciofi-Baffoni S, Banci L (2020) GLRX3 acts as a [2Fe–2S] cluster chaperone in the cytosolic iron–sulfur assembly machinery transferring [2Fe–2S] clusters to NUBP1. *J Am Chem Soc* 142(24):10794–10805. <https://doi.org/10.1021/jacs.0c02266>
  14. Dicus MM, Conlan A, Nechushtai R, Jennings PA, Paddock ML, Britt RD, Stoll S (2010) Binding of histidine in the (Cys)(3)(His)(1)-coordinated [2Fe–2S] cluster of human mitoNEET. *J Am Chem Soc* 132(6):2037–2049. <https://doi.org/10.1021/ja909359g>
  15. Tamir S, Paddock ML, Darash-Yahana-Baram M, Holt SH, Sohn YS, Agranat L, Michaeli D, Stofleth JT, Lipper CH, Morcos F, Cabantchik IZ, Onuchic JN, Jennings PA, Mittler R, Nechushtai R (2015) Structure-function analysis of NEET proteins uncovers their role as key regulators of iron and ROS homeostasis in health and disease. *Biochim Biophys Acta Mol Cell Res* 1853(6):1294–1315. <https://doi.org/10.1016/j.bbamcr.2014.10.014>
  16. Bak DW, Elliott SJ (2013) Conserved hydrogen bonding networks of mitoNEET tune Fe–S cluster binding and structural stability. *Biochemistry* 52(27):4687–4696. <https://doi.org/10.1021/bi400540m>
  17. Pesce L, Calandrini V, Marjault HB, Lipper CH, Rossetti G, Mittler R, Jennings PA, Bauer A, Nechushtai R, Carloni P (2017) Molecular dynamics simulations of the [2Fe–2S] cluster-binding domain of NEET proteins reveal key molecular determinants that induce their cluster transfer/release. *J Phys Chem B* 121(47):10648–10656. <https://doi.org/10.1021/acs.jpcc.7b10584>
  18. Baker FN, Porollo A (2016) CoeViz: a web-based tool for coevolution analysis of protein residues. *BMC Bioinform* 17(1):1–7. <https://doi.org/10.1186/s12859-016-0975-z>
  19. Stephens PJ, Devlin FJ, Chabalowski CF, Frisch MJ (1994) Ab-initio calculation of vibrational absorption and circular-dichroism spectra using density-functional folded force-fields. *J Phys Chem* 98(45):11623–11627. <https://doi.org/10.1021/j100096a001>
  20. Lee CT, Yang WT, Parr RG (1988) Development of the Colle–Salvetti correlation-energy formula into a functional of the electron-density. *Phys Rev B* 37(2):785–789. <https://doi.org/10.1103/PhysRevB.37.785>
  21. Carvalho ATP, Teixeira AFS, Ramos MJ (2013) Parameters for molecular dynamics simulations of iron–sulfur proteins. *J Comput Chem* 34(18):1540–1548. <https://doi.org/10.1002/jcc.23287>
  22. Paddock ML, Wiley SE, Axelrod HL, Cohen AE, Roy M, Abresch EC, Capraro D, Murphy AN, Nechushtai R, Dixon JE, Jennings PA (2007) MitoNEET is a uniquely folded 2Fe–2S outer mitochondrial membrane protein stabilized by pioglitazone. *Proc Natl Acad Sci USA* 104(36):14342–14347. <https://doi.org/10.1073/pnas.0707189104>
  23. Becke AD (1988) Density-functional exchange-energy approximation with correct asymptotic-behavior. *Phys Rev A* 38(6):3098–3100. <https://doi.org/10.1103/PhysRevA.38.3098>
  24. Perdew JP (1986) Density-functional approximation for the correlation-energy of the inhomogeneous electron-gas. *Phys Rev B* 33(12):8822–8824. <https://doi.org/10.1103/PhysRevB.33.8822>
  25. Outeiral C, Vincent MA, Pendas AM, Popelier PLA (2018) Revitalizing the concept of bond order through delocalization measures in real space. *Chem Sci* 9(25):5517–5529. <https://doi.org/10.1039/C8SC01338A>
  26. Harris TV, Szilagyi RK (2014) Iron–sulfur bond covalency from electronic structure calculations for classical iron–sulfur clusters. *J Comput Chem* 35(7):540–552. <https://doi.org/10.1002/jcc.23518>
  27. Lonsdale R, Harvey JN, Mulholland AJ (2012) Effects of dispersion in density functional based quantum mechanical/molecular mechanical calculations on cytochrome P450 catalyzed reactions. *J Chem Theory Comput* 8(11):4637–4645. <https://doi.org/10.1021/ct300329h>
  28. Lei H, Guo YB, Hu XD, Hu CG, Hu XT, Li HB (2017) Reversible unfolding and folding of the metalloprotein ferredoxin revealed by single-molecule atomic force microscopy. *J Am Chem Soc* 139(4):1538–1544. <https://doi.org/10.1021/jacs.6b11371>
  29. Rose K, Shadle SE, Glaser T, de Vries S, Cherepanov A, Canters GW, Hedman B, Hodgson KO, Solomon EI (1999) Investigation of the electronic structure of 2Fe–2S model complexes and the Rieske protein using ligand K-edge X-ray absorption spectroscopy. *J Am Chem Soc* 121(11):2353–2363. <https://doi.org/10.1021/ja9834551>
  30. Lu T, Chen QX (2020) A simple method of identifying  $\pi$  orbitals for non-planar systems and a protocol of studying  $\pi$  electronic structure. *Theor Chem Acc* 139(2):1–12. <https://doi.org/10.1007/s00214-019-2541-z>
  31. Grimme S (2006) Semiempirical GGA-type density functional constructed with a long-range dispersion correction. *J Comput Chem* 27(15):1787–1799. <https://doi.org/10.1002/jcc.20495>
  32. Grimme S, Antony J, Ehrlich S, Krieg H (2010) A consistent and accurate ab initio parametrization of density functional dispersion correction (DFT-D) for the 94 elements H–Pu. *J Chem Phys* 132(15):154104. <https://doi.org/10.1063/1.3382344>
  33. Bowman SEJ, Bren KL (2010) Variation and analysis of second-sphere interactions and axial histidinate character in c-type




- cytochromes. *Inorg Chem* 49(17):7890–7897. <https://doi.org/10.1021/ic100899k>
34. Shirmanova MV, Druzhkova IN, Lukina MM, Matlashov ME, Belousov VV, Snopova LB, Prodanetz NN, Dudenkova VV, Lukyanov SA, Zagaynova EV (2015) Intracellular pH imaging in cancer cells in vitro and tumors in vivo using the new genetically encoded sensor SypHer2. *Biochim Biophys Acta Gen Subj* 1850(9):1905–1911. <https://doi.org/10.1016/j.bbagen.2015.05.001>
  35. Baxter EL, Zuris JA, Wang C, Vo PLT, Axelrod HL, Cohen AE, Paddock ML, Nechushtai R, Onuchic JN, Jennings PA (2013) Allosteric control in a metalloprotein dramatically alters function. *Proc Natl Acad Sci USA* 110(3):948–953. <https://doi.org/10.1073/pnas.1208286110>
  36. Suel GM, Lockless SW, Wall MA, Ranganathan R (2003) Evolutionarily conserved networks of residues mediate allosteric communication in proteins. *Nat Struct Mol Biol* 10(1):59–69. <https://doi.org/10.1038/nsb881>
  37. Karmi O, Marjault HB, Pesce L, Carloni P, Onuchic JN, Jennings PA, Mittler R, Nechushtai R (2018) The unique fold and lability of the [2Fe–2S] clusters of NEET proteins mediate their key functions in health and disease. *J Biol Inorg Chem* 23(4):599–612. <https://doi.org/10.1007/s00775-018-1538-8>
  38. Li P, Merz KM (2016) MCPB.py: a python based metal center parameter builder. *J Chem Inf Model* 56(4):599–604. <https://doi.org/10.1021/acs.jcim.5b00674>
  39. Case DA, Betz RM, Cerutti DS, Cheatham TE III, Darden TA, Duke RE, Giese TJ, Gohlke H, Goetz AW, Homeyer N, Izadi S, Janowski P, Kaus J, Kovalenko A, Lee TS, LeGrand S, Li P, Lin C, Luchko T, Luo R, Madej B, Mermelstein D, Merz KM, Monard G, Nguyen H, Nguyen HT, Omelyan I, Onufriev A, Roe DR, Roitberg A, Sagui C, Simmerling CL, Botello-Smith WM, Swails J, Walker RC, Wang J, Wolf RM, Wu X, Xiao L, Kollman PA (2016) AMBER 2016. University of California, San Francisco. <https://doi.org/10.13140/RG.2.2.27958.70729>
  40. Hou XW, Liu RJ, Ross S, Smart EJ, Zhu HN, Gong WM (2007) Crystallographic studies of human mitoNEET. *J Biol Chem* 282(46):33242–33246. <https://doi.org/10.1074/jbc.C700172200>
  41. Conlan AR, Paddock ML, Axelrod HL, Cohen AE, Abresch EC, Wiley S, Roy M, Nechushtai R, Jennings PA (2009) The novel 2Fe–2S outer mitochondrial protein mitoNEET displays conformational flexibility in its N-terminal cytoplasmic tethering domain. *Acta Crystallogr Sect F Struct Biol Cryst Commun* 65(7):654–659. <https://doi.org/10.1107/S1744309109019605>
  42. Lin J, Zhou T, Ye K, Wang J (2007) Crystal structure of human mitoNEET reveals distinct groups of iron sulfur proteins. *Proc Natl Acad Sci USA* 104(37):14640–14645. <https://doi.org/10.1073/pnas.0702426104>
  43. Arif W, Xu S, Isailovic D, Geldenhuys WJ, Carroll RT, Funk MO (2011) Complexes of the outer mitochondrial membrane protein MitoNEET with resveratrol-3-sulfate. *Biochemistry* 50(25):5806–5811. <https://doi.org/10.1021/bi200546s>
  44. Geldenhuys WJ, Long TE, Saralkar P, Iwasaki T, Nunez RAA, Nair RR, Konkle ME, Menze MA, Pinti MV, Hollander JM, Hazlehurst LA, Robart AR (2019) Crystal structure of the mitochondrial protein mitoNEET bound to a benze-sulfonide ligand. *Commun Chem* 2(1):77. <https://doi.org/10.1038/s42004-019-0172-x>
  45. Tamir S, Eisenberg-Domovich Y, Conlan AR, Stoffleth JT, Lipper CH, Paddock ML, Mittler R, Jennings PA, Livnah O, Nechushtai R (2014) A point mutation in the [2Fe–2S] cluster binding region of the NAF-1 protein (H114C) dramatically hinders the cluster donor properties. *Acta Crystallogr D Biol Crystallogr* 70(6):1572–1578. <https://doi.org/10.1107/S1399004714005458>
  46. Conlan AR, Axelrod HL, Cohen AE, Abresch EC, Zuris J, Yee D, Nechushtai R, Jennings PA, Paddock ML (2009) Crystal structure of Miner1: the redox-active 2Fe–2S protein causative in Wolfram Syndrome 2. *J Mol Biol* 392(1):143–153. <https://doi.org/10.1016/j.jmb.2009.06.079>
  47. Frisch MJ, Trucks GW, Schlegel HB, Scuseria GE, Robb MA, Cheeseman JR, Scalmani G, Barone V, Mennucci B, Petersson GA, Nakatsuji H, Caricato M, Li X, Hratchian HP, Izmaylov AF, Bloino J, Zheng G, Sonnenberg JL, Hada M, Ehara M, Toyota K, Fukuda R, Hasegawa J, Ishida M, Nakajima T, Honda Y, Kitao O, Nakai H, Vreven T, Montgomery Jr JA, Peralta JE, Ogliaro F, Bearpark M, Heyd JJ, Brothers E, Kudin KN, Staroverov VN, Kobayashi R, Normand J, Raghavachari K, Rendell A, Burant JC, Iyengar SS, Tomasi J, Cossi M, Rega N, Millam JM, Klene M, Knox JE, Cross JB, Bakken V, Adamo C, Jaramillo J, Gomperts R, Stratmann RE, Yazyev O, Austin AJ, Cammi R, Pomelli C, Ochterski JW, Martin RL, Morokuma K, Zakrzewski VG, Voth GA, Salvador P, Dannenberg JJ, Dapprich S, Daniels AD, Farkas O, Foresman JB, Ortiz JV, Cioslowski J, Fox DJ (2009) Gaussian 09 Rev. A.02. Wallingford
  48. Sandala GM, Hopmann KH, Ghosh A, Noodleman L (2011) Calibration of DFT functionals for the prediction of Fe-57 Mossbauer spectral parameters in iron–nitrosyl and iron–sulfur complexes: accurate geometries prove essential. *J Chem Theory Comput* 7(10):3232–3247. <https://doi.org/10.1021/ct200187d>
  49. Ha Y, Arnold AR, Nunez NN, Bartels PL, Zhou A, David SS, Barton JK, Hedman B, Hodgson K, Solomon EI (2017) Sulfur K-edge XAS studies of the effect of DNA binding on the [Fe4S4] site in EndoIII and MutY. *J Am Chem Soc* 139(33):11434–11442. <https://doi.org/10.1021/jacs.7b03966>
  50. Capelli R, Lyu W, Bolnykh V, Meloni S, Magnus J, Olsen H, Rothlisberger U, Parrinello M, Carloni P (2020) Accuracy of molecular simulation-based predictions of  $k_{\text{off}}$  values: a metadynamics study. *J Phys Chem Lett* 11(15):6373–6381. <https://doi.org/10.1021/acs.jpclett.0c00999>
  51. Porollo AA, Adamczak R, Meller J (2004) POLYVIEW: a flexible visualization tool for structural and functional annotations of proteins. *Bioinformatics* 20(15):2460–2462. <https://doi.org/10.1093/bioinformatics/bth248>
  52. Burger L, van Nimwegen E (2010) Disentangling direct from indirect co-evolution of residues in protein alignments. *PLoS Comput Biol* 6(1):e1000633. <https://doi.org/10.1371/journal.pcbi.1000633>
  53. Gordon JC, Myers JB, Foltz T, Shoja V, Heath LS, Onufriev A (2005) H++: a server for estimating pK(a)s and adding missing hydrogens to macromolecules. *Nucleic Acids Res* 33(suppl\_2):W368–W371. <https://doi.org/10.1093/nar/gki464>
  54. Lindorff-Larsen K, Piana S, Palmo K, Maragakis P, Klepeis JL, Dror RO, Shaw DE (2010) Improved side-chain torsion potentials for the Amber ff99SB protein force field. *Proteins* 78(8):1950–1958. <https://doi.org/10.1002/prot.22711>
  55. Sorin EJ, Pande VS (2005) Exploring the helix-coil transition via all-atom equilibrium ensemble simulations. *Biophys J* 88(4):2472–2493. <https://doi.org/10.1529/biophysj.104.051938>
  56. Jorgensen WL, Chandrasekhar J, Madura JD, Impey RW, Klein ML (1983) Comparison of simple potential functions for simulating liquid water. *J Chem Phys* 79(2):926–935. <https://doi.org/10.1063/1.445869>
  57. Aqvist J (1990) Ion water interaction potentials derived from free-energy perturbation simulations. *J Phys Chem* 94(21):8021–8024. <https://doi.org/10.1021/j100384a009>
  58. Bayly CI, Cieplak P, Cornell WD, Kollman PA (1993) A well-behaved electrostatic potential based method using charge restraints for deriving atomic charges—the RESP model. *J Phys Chem* 97(40):10269–10280. <https://doi.org/10.1021/j100142a004>
  59. Cieplak P, Cornell WD, Bayly C, Kollman PA (1995) Application of the multimolecule and multiconformational RESP methodology to biopolymers—charge derivation for DNA, RNA, and



- proteins. *J Comput Chem* 16(11):1357–1377. <https://doi.org/10.1002/jcc.540161106>
60. Essmann U, Perera L, Berkowitz ML, Darden T, Lee H, Pedersen LG (1995) A smooth particle mesh Ewald method. *J Chem Phys* 103(19):8577–8593. <https://doi.org/10.1063/1.470117>
  61. Hess B, Bekker H, Berendsen HJC, Fraaije JGEM (1997) LINCS: a linear constraint solver for molecular simulations. *J Comput Chem* 18(12):1463–1472. [https://doi.org/10.1002/\(SICI\)1096-987X\(199709\)18:12%3C1463::AID-JCC4%3E3.0.CO;2-H](https://doi.org/10.1002/(SICI)1096-987X(199709)18:12%3C1463::AID-JCC4%3E3.0.CO;2-H)
  62. Nose S (1984) A molecular-dynamics method for simulations in the canonical ensemble. *Mol Phys* 52(2):255–268. <https://doi.org/10.1080/00268978400101201>
  63. Hoover WG (1985) Canonical dynamics—equilibrium phase-space distributions. *Phys Rev A* 31(3):1695–1697. <https://doi.org/10.1103/PhysRevA.31.1695>
  64. Parrinello M, Rahman A (1981) Polymorphic transitions in single-crystals—a new molecular-dynamics method. *J Appl Phys* 52(12):7182–7190. <https://doi.org/10.1063/1.328693>
  65. Daura X, Gademann K, Jaun B, Seebach D, van Gunsteren WF, Mark AE (1999) Peptide folding: when simulation meets experiment. *Angew Chem Int Edit* 38(1–2):236–240. [https://doi.org/10.1002/\(SICI\)1521-3773\(19990115\)38:1/2%3C236::AID-ANIE236%3E3.0.CO;2-M](https://doi.org/10.1002/(SICI)1521-3773(19990115)38:1/2%3C236::AID-ANIE236%3E3.0.CO;2-M)
  66. Dennington R, Keith T, Millam J (2009) GaussView, Version 5. Semichem Inc., Shawnee Mission
  67. Lu T, Chen FW (2012) Multiwfn: a multifunctional wavefunction analyzer. *J Comput Chem* 33(5):580–592. <https://doi.org/10.1002/jcc.22885>
  68. Berendsen HJC, Vanderspoel D, Vandrunen R (1995) GROMACS—a message-passing parallel molecular-dynamics implementation. *Comput Phys Commun* 91(1–3):43–56. [https://doi.org/10.1016/0010-4655\(95\)00042-E](https://doi.org/10.1016/0010-4655(95)00042-E)
  69. Abraham MJ, Murtola T, Schulz R, Páll S, Smith JC, Hess B, Lindahl E (2015) GROMACS: high performance molecular simulations through multi-level parallelism from laptops to supercomputers. *SoftwareX* 1–2:19–25. <https://doi.org/10.1016/j.softx.2015.06.001>

**Publisher's Note** Springer Nature remains neutral with regard to jurisdictional claims in published maps and institutional affiliations.

## Authors and Affiliations

Ke Zuo<sup>1,2</sup>  · Henri-Baptiste Marjault<sup>1,2</sup>  · Kara L. Bren<sup>3</sup>  · Giulia Rossetti<sup>4,5,6</sup> · Rachel Nechushtai<sup>1</sup>  · Paolo Carloni<sup>2,4,7</sup> 

<sup>1</sup> The Alexander Silberman Institute of Life Science, The Hebrew University of Jerusalem, Edmond J. Safra Campus at Givat Ram, 91904 Jerusalem, Israel

<sup>2</sup> Department of Physics, RWTH Aachen University, 52074 Aachen, Germany

<sup>3</sup> Department of Chemistry, University of Rochester, Rochester, NY 14627-0216, USA

<sup>4</sup> Computational Biomedicine, Institute of Advanced Simulation IAS-5 and Institute of Neuroscience and Medicine INM-9, Forschungszentrum Jülich GmbH, 52425 Jülich, Germany

<sup>5</sup> Jülich Supercomputing Center (JSC), Forschungszentrum Jülich GmbH, Jülich, Germany

<sup>6</sup> Department of Neurology, Faculty of Medicine, RWTH Aachen University, 52074 Aachen, Germany

<sup>7</sup> JARA Institute: Molecular Neuroscience and Imaging, Institute of Neuroscience and Medicine INM-11, Forschungszentrum Jülich GmbH, 52425 Jülich, Germany